

MIT Open Access Articles

Elucidating Relayed Proton Transfer through a His-Trp-His Triad of a Transmembrane Proton Channel by Solid-State NMR

The MIT Faculty has made this article openly available. **Please share** how this access benefits you. Your story matters.

As Published: 10.1016/J.JMB.2019.05.009

Publisher: Elsevier BV

Persistent URL: <https://hdl.handle.net/1721.1/135177>

Version: Author's final manuscript: final author's manuscript post peer review, without publisher's formatting or copy editing

Terms of use: Creative Commons Attribution-NonCommercial-NoDerivs License





Published in final edited form as:

J Mol Biol. 2019 June 28; 431(14): 2554–2566. doi:10.1016/j.jmb.2019.05.009.

Elucidating Relayed Proton Transfer Through a His-Trp- His Triad of a Transmembrane Proton Channel by Solid-State NMR

Byungsu Kwon[§], Matthias Roos[§], Venkata S. Mandala, Alexander A. Shcherbakov, and Mei Hong

Department of Chemistry, Massachusetts Institute of Technology, 170 Albany Street, Cambridge, MA 02139

Abstract

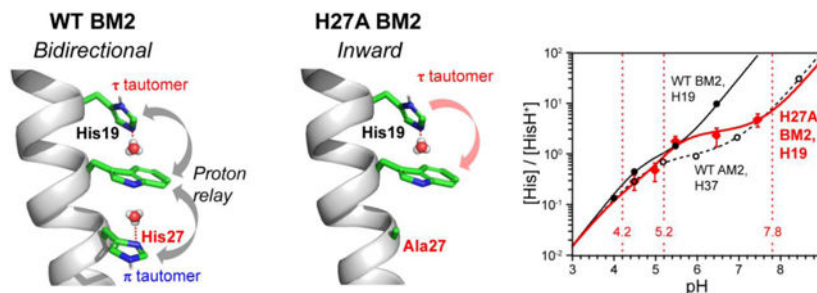
Proton transfer in membrane-bound ion channels is mediated by both water and polar residues of proteins, but the detailed molecular mechanism is challenging to determine. The tetrameric influenza A and B virus M2 proteins form canonical proton channels that use an HxxxW motif for proton selectivity and gating. The BM2 channel also contains a second histidine (His), H27, equidistant from the gating tryptophan, which leads to a symmetric H¹⁹xxxW²³xxxH²⁷ motif. The proton-dissociation constants (pK_a's) of H19 in BM2 were found to be much lower than the pK_a's of H37 in AM2. To determine if the lower pK_a's result from H27-facilitated proton dissociation of H19, we have now investigated a H27A mutant of BM2 using solid-state NMR. ¹⁵N NMR spectra indicate that removal of the second histidine converted the protonation and tautomeric equilibria of H19 to be similar to the H37 behavior in AM2, indicating that the peripheral H27 is indeed the origin of the low pK_a's H19 in wild-type BM2. Measured interhelical distances between W23 sidechains indicate that the pore constriction at W23 increases with the H19 tetrad charge but is independent of the H27 mutation. These results indicate that H27 both accelerates proton dissociation from H19 to increase the inward proton conductance, and causes the small reverse conductance of BM2. The proton relay between H19 and H27 is likely mediated by the intervening gating tryptophan through cation- π interactions. This relayed proton transfer may exist in other ion channels and has implications for the design of imidazole-based synthetic proton channels.

Graphical abstract

Corresponding author: Mei Hong, Tel: 617-253-5521, meihong@mit.edu.

[§]: These authors contributed equally to this work.

Publisher's Disclaimer: This is a PDF file of an unedited manuscript that has been accepted for publication. As a service to our customers we are providing this early version of the manuscript. The manuscript will undergo copyediting, typesetting, and review of the resulting proof before it is published in its final citable form. Please note that during the production process errors may be discovered which could affect the content, and all legal disclaimers that apply to the journal pertain.



Keywords

Influenza M2; ^{19}F CODEX; proton dissociation constant; proton transport; magic-angle spinning NMR

Introduction

Proton transfer in ion channels is commonly mediated by polar residues in conjunction with water. For example, the voltage-gated proton channels (H_V) contain a conserved RxWRxxR motif [1, 2], in which Trp mutation increases channel opening and closing by two orders of magnitude and disrupt the pH dependence of gating [3]. In human carbonic anhydrase II, His64 plays a role in proton transfer over a long distance from the active site to the solvent during enzyme turnover [4, 5]. For membrane-bound ion channels, high-resolution structural information about the kinetics and equilibria of polar-sidechain mediated proton transfer is challenging to obtain because of the invisibility of protons to crystallography and the difficulty of measuring protein motion in lipid membranes. For this reason, the small proton-selective M2 channel of influenza A and B viruses represents an excellent system for elucidating atomic details of proton transfer. After the virus enters the acidic endosome of the host cell, the low pH activates the tetrameric M2 channel, which triggers viral uncoating [6–8]. The amantadine family of influenza A M2 (AM2) inhibitors is now ineffective due to widespread resistance as a result of protein mutation at the drug binding pocket [9], whereas no BM2 inhibitors have been developed because of the very different amino acid sequence of BM2: the BM2 channel pore is lined with polar residues whereas the AM2 channel pore is lined with hydrophobic residues. The two proteins share only a conserved HxxxW motif in the transmembrane (TM) domain, where His is responsible for proton selectivity [10] while Trp is responsible for asymmetric proton conduction from the N-terminus to the C-terminus (inward proton flux) [11]. The analogous position to H19 in BM2 is H37 in AM2, and W23 in BM2 corresponds to W41 in AM2 (Fig. 1A).

Extensive solid-state NMR data and crystal structures of water-permeated pores of M2 proteins indicate that water transfers protons to and from the proton-selective H37 in AM2 [12–15]. This exchange occurs on the microsecond timescale [16, 17]. As the pH decreases, the histidine tetrad increasingly protonates, where four proton dissociation constants (pK_a 's) have been measured using ^{15}N NMR spectra of the imidazole sidechains [16, 18, 19]. Interestingly, these pH-dependent ^{15}N spectra indicate that BM2 H19 has much lower pK_a 's compared to AM2 H37 [20]. At pH 5.5, the average H19 tetrad charge is 1.5 ± 0.1 in BM2

whereas the average H37 tetrad charge is 2.2 ± 0.1 in AM2. One hypothesis to explain this significant difference is that the second histidine in BM2, H27, facilitates H19 deprotonation. These two histidine residues are equidistant from W23, thus giving a unique symmetric $H^{19}xxxW^{23}xxxH^{27}$ motif (Fig. 1A, B). This motif is absent in AM2 because the corresponding residue, R45, is not titratable. H27 ^{15}N NMR spectra showed that H27 protonates with much higher pK_a 's of 7.9 and 5.9 [21], consistent with the hypothesis that H27 may mediate proton dissociation from H19, hence decreasing its pK_a 's. An auxiliary role of H27 in BM2 proton conduction is also implied by electrophysiological data that H27A and H27C mutants have reduced but non-zero conductance [22, 23].

Structural and biochemical studies gave other clues about the potential role of the $HxxxWxxxH/R$ motif for proton conduction in M2. Solid-state NMR data of a W41F mutant of AM2 indicate that W41 prevents C-terminal hydronium ions from protonating H37 [24], thus ensuring unidirectional proton conduction from the N-terminus to the C-terminus. Electrophysiological data of a D44N mutant of AM2 indicate that W41 is stabilized by D44 [25, 26], while the equivalent residue G26 in BM2 is unlikely to accomplish this task for W23 due to its inability to form hydrogen bonds. Indeed, BM2 shows a small reverse current unless both G26 and H27 are mutated [27]. These data suggest that the precise conformation of the Trp gate and the positive charges at the C-terminus of the TM helix may dictate the presence or absence of outward proton flux in influenza M2 channels.

To elucidate whether the altered protonation equilibria of H19 is indeed due to proton relay from H19 to H27, and to understand the origin of the different conductance asymmetry between AM2 and BM2, we have now studied the H27A mutant BM2 using solid-state NMR (Fig. 1C). This mutant has been shown to exhibit 30–40% lower conductance compared to wild-type (WT) BM2 [22, 23]. We show that H19 in the mutant adopts the protonation phenotype of WT AM2, thus conclusively proving that H27 is responsible for lowering the H19 pK_a 's. This result in turn suggests that protons are relayed from H19 to H27. The measured tautomeric equilibrium of H19 in the mutant suggests that protons are conducted more unidirectionally in the mutant than in the WT channel. Finally, we present interhelical distance data and channel hydration data to shed light on how the peripheral H27 affects the channel diameter at neutral and acidic pH.

Results and Discussion

pH-dependent conformations of H19 differ between the mutant and wild-type BM2

We first investigated the conformation of H27A BM2 by measuring site-specific chemical shifts. Fig. S1 shows ^{13}C cross-polarization (CP) MAS spectra of the peptide bound to a virus-mimetic membrane (VM+) from pH 7.5 to 4.5. Residues S12, I14 and A22 exhibit pH-independent α -helical chemical shifts for $C\alpha$ and $C\beta$. These chemical shifts are indistinguishable from the chemical shifts of WT BM2 [20, 21], indicating that the H27A mutation has little effect on the backbone conformation of the TM domain.

In comparison, the proton-selective H19 shows multiple $C\alpha$ – $C\beta$ correlation peaks whose chemical shifts vary with pH (Fig. 2 and Fig. S2). These $C\alpha$ – $C\beta$ cross peaks can be assigned to neutral τ and π tautomers and cationic species based on their correlations with the

imidazole C γ and C δ 2 chemical shifts [13, 16, 20]. The neutral histidine peaks are assigned to τ_0 to τ_3 states and π_0 to π_3 states, where the subscripts refer to the dominant charge state of the H19 tetrad at the various pH, as determined using ^{15}N NMR (*vide infra*). Using this nomenclature, τ - and π - tautomer peaks with the same chemical shifts but a different charge of the tetramer have different subscripts, for example, τ_1 at pH 6.5 versus τ_2/τ_3 at pH 5.0. At pH 7.5, four C α –C β cross peaks are observed (Fig. 2A), two belonging to τ tautomers and two to π tautomers: the former correlate with a C δ 2 peak at 113–114 ppm whereas the latter correlate with a C δ 2 peak at 124 ppm (Table S1). In addition to neutral tautomers, several cationic species are observed at acidic pH. At pH 6.5, the +1 tetrad population is dominant (*vide infra*), thus we assigned the (57.9, 30.0) ppm peak to the *cat1* state, even though the correlated aromatic chemical shifts are similar to those of the τ_0 tautomer. The total intensities of the τ_1 and π_1 peaks are about 3-fold larger than the *cat1* intensities, consistent with the fact that the +1 tetrad dominates at this pH (Fig. 2B, Fig. 3C). At pH 5.0, new C α –C β cross peaks appear and can be assigned to *cat2* and *cat3* states on the basis of their correlations with C δ 2 chemical shifts of 117–118 ppm.

In total, we resolved four τ tautomer species and four π species over the full pH range examined (Table S1). This structural polymorphism differs qualitatively from wild-type AM2 and BM2, which exhibit a single τ and π tautomer [13, 16, 20]. The chemical shift differences within each tautomer are significant: for example, the τ_1 and τ_0 states differ by 4.6 ppm in their C α chemical shifts and the π_1 and π_0 tautomers show a similarly large C α chemical shift difference of 5.0 ppm (Fig. 2A, B). At more acidic pH, the chemical shifts of the neutral tautomers change further. These results indicate that the charge state of the surrounding helices exerts a significant influence on the conformation of a helix, so that imidazole rings of the same chemical structure can be associated with helical backbones with different (ϕ , ψ) angles and possibly different (χ_1 , χ_2) angles.

At acidic pH, the π tautomers have weaker intensities than the τ tautomers, and no π_3/π_2 peaks are observed at pH 4.5 (Fig. S3). The higher population of the τ tautomer over the π tautomer is also observed in AM2, and is correlated with asymmetric proton conduction from the N- to the C-terminus [24]. Interestingly, the *cat2/cat3* chemical shifts at pH 4.5 differ slightly from those measured at pH 5, thus we denote these by *cat2'/cat3'*. We attribute this difference to the lack of π tautomers at pH 4.5, and suggest that charge repulsion as well as the altered tautomer equilibrium of neutral histidines in the same tetrad affect the conformation of the cationic histidines. Since residues S12, I14 and A22 show no significant chemical shift changes with pH, and the residues neighboring H19 contain no titratable groups, the helix backbone conformation is not affected by pH. Thus, the altered conformation of the cationic histidines must largely result from the structural changes in the imidazole tetrad. Longer-range interactions with W23 may additionally reinforce or counteract the effect.

H19 in the mutant protonates in a hybrid manner between wild-type BM2 and AM2

To investigate whether H27 facilitates proton dissociation from H19 to increase the proton conductance [21], we measured the charge-state distribution of H19 in the mutant channel using ^{15}N NMR (Fig. 3). If H27 indeed siphons protons from H19, then the H27A mutation

should shift the H19 equilibrium to the cationic state, thus increasing its pK_a 's. Quantitative ^{15}N NMR spectra of the imidazole ring report how the relative intensities of the unprotonated $\text{N}\delta 1^\tau/\text{N}\epsilon 2^\pi$ peak at ~250 ppm and the protonated peaks at 160–180 ppm vary with pH. The latter include the 170-ppm $\text{N}\delta 1\text{H}^\pi$ and 165-ppm $\text{N}\epsilon 2\text{H}^\tau$ neutral tautomer signals as well as the cationic His signal at 175 ppm. At pH 4.5 and 5.5, H19 in the mutant BM2 has similar intensity distributions as that in the WT peptide (Fig. 3A), but at pH 6.5 the mutant has much lower intensity for the unprotonated peak than the WT BM2, indicating that H19 retains its positive charge to higher pH when H27 is mutated to Ala.

To quantify the H19 pK_a 's in the mutant BM2 channel, we extracted the neutral-to-cationic H19 concentration ratios from the integrated ^{15}N peak intensities after correcting for the ^1H – ^{15}N CP efficiency (Table S2). At the lowest pH of 4.5, H19 in the mutant channel has a similar intensity ratio as H19 in WT BM2 or H37 in WT AM2 (Fig. 3B). As pH increases, the mutant H19 retains its cationic charges better than in WT BM2. For example, at pH 6.5, the mutant BM2 has 4-fold larger cationic charges than WT BM2, whereas WT AM2 has 10-fold higher charge than WT BM2 (Table S2) [16, 20]. Therefore, the proton-selective His in the mutant transitions from the WT BM2 behavior to the AM2 behavior at around pH 6.5. At pH 7.5 or higher, the H19 protonation state in the mutant BM2 is indistinguishable from the H37 protonation state in WT AM2. Since all three M2 channels have similarly high charge states at very low pH, the main distinction lies at intermediate and high pH, where H19 in the mutant BM2 behaves essentially like WT AM2.

These quantitative ^{15}N NMR spectra yielded four H19 pK_a values of 4.2 ± 0.4 , 5.2 ± 0.2 , 5.2 ± 0.2 , and 7.8 ± 0.3 for the mutant BM2 (Fig. 3C). Interestingly, the average pK_a value of 5.6 lies between the average pK_a of H19 (5.1) and H27 (6.4) in the WT channel [21]. For comparison, the average pK_a of H37 in AM2 is 5.9 [16], which is close to the average H19 pK_a of the mutant BM2.

It is informative to compare the populations of the charged histidine tetrads in the three M2 peptides (Fig. 3D–G; see Fig. S4 for overlaid profiles). At pH 6.5, WT AM2 and BM2 carry the same average total charge, but most of the charges in BM2 are concentrated at the membrane-surface H27. The average charge of H37 is 1.6 ± 0.1 , whereas the average BM2 charge is 0.4 ± 0.1 at H19 and 1.3 ± 0.1 at H27. In mutant BM2, H19 carries an average charge of +1 at pH 6.5. The similar total charges of these channels, regardless of whether there is a single histidine or two histidines in the TM helix, suggest a negative cooperativity in proton dissociation in the dual-histidine WT BM2, where H27 protonation promotes deprotonation of H19.

The negative cooperativity between the two histidines of BM2 is further supported by a comparison of the charge distribution within the histidine tetrad (Fig. S4). At low pH, the charge population of H19 in the mutant BM2 is similar to that of H19 in WT BM2, with only minor contributions of the second histidine, H27, to the charge state of H19. However, at pH > 6.5, H19 is essentially neutral in WT BM2 but remains cationic in the mutant. Thus, there is a transition from weak to strong contributions of H27 to the charge release at H19 with increasing pH. Comparing the charge distribution pattern of H19 in the mutant BM2 and H37 in WT AM2, both possessing only a single histidine in the TM domain, we find

that the +4, +3 and +0 tetrads have the same pH dependence and the same charge populations in the two peptides. Differences occur for the +1 and +2 states: the AM2 channel is dominated by the +2-state at pH 6 while the mutant BM2 exists mostly as a +1 tetramer at the same pH. This difference can be attributed to the slowed proton release in the mutant BM2 at neutral pH compared to WT AM2 (Fig. 3B).

Although the charge distribution of H19 in WT BM2 and H37 in AM2 differ most drastically at neutral pH, the two WT channels still carry the same total charge: the H37 tetrad carries an average charge of 0.7 ± 0.1 at pH 7.5, whereas WT BM2 carries essentially no charge at H19 but 0.7 ± 0.1 charges at H27. In the H27A BM2 mutant, the total charge is 0.7 ± 0.1 at pH 7.5 as well, and is exclusively located on H19. Since all charges were essentially transferred from H19 to H27, we expect H27 in WT BM2 to exhibit a similar charge population as H19 in mutant BM2. A comparison of the charge population curves (Fig. S4B) confirms this statement: for $\text{pH} > 6.5$, the charge distribution patterns of H19 in mutant BM2 and H27 in WT BM2 are essentially identical. These quantitative results support the presence of proton relay from the first His (H19) to the second His (H27), and are consistent with recent findings from molecular dynamics simulations that suggest an activation-promotion mechanism in which H27 protonation decreases the energy barrier for H19 deprotonation [28]. Since the $\text{Ca}-\text{Ca}$ distance between the two residues is long, $\sim 11 \text{ \AA}$, the H19–H27 interactions are most likely mediated by cation– π interactions through the intervening W23 [29].

Increased channel hydration at low pH correlates with the H19 tetrad charge

Water accessibility and proton exchange rates between the protein and water provide information about channel hydration. WT BM2 shows higher hydration at low pH than at high pH, consistent with channel activation [20]. Since the H27A mutation removed the C-terminal charge, we wonder whether the mutant is less hydrated than the WT BM2 at the same pH, and whether the C-terminus is less hydrated than the N-terminus in the mutant. To answer these questions, we measured ^{13}C -detected water-to-protein ^1H spin diffusion spectra at 30 kHz MAS. We used a ^1H spin exchange mixing time of 9 ms (S) to measure the initial polarization transfer to the protein and 100 ms (S_0) to measure the equilibrium polarization transfer (Fig. 4A). The S_0 spectra at various pH have the same relative intensities for the protein signals as the ^{13}C CP spectra, but the total spectral intensities are reduced to 20–25% of the CP spectra. This value is consistent with the fact that water accounts for 45–55% of all protons in our membrane samples. Thus, when uniformly distributed across the entire sample, water-transfer ^1H magnetization should give $\sim 25\%$ of the total unfiltered ^1H magnetization. Because the lipid ^{13}C signals are mostly suppressed in the water-transferred S_0 and S spectra, which facilitate spectral analysis, we use the 100 ms S_0 spectra to normalize the initial-regime S spectra. The S/S_0 intensity ratios reflect three factors: the channel hydration level, the hydrogen exchange rates, and the ^1H spin diffusion rates within the protein. Water-to-protein proton exchange occurs most efficiently at sidechains containing labile NH- or OH-groups. In the TM heptad repeat, residues E3, S9, S12, H19, W23, H27, Q30, and R33 are expected to line the hydrated pore (Fig. 1A and Fig. 4B). Residue E3 at the dynamic N-terminus should have inefficient ^1H spin diffusion and thus only minor effects on the S/S_0 values of the other TM residues. This leaves S12 and

H19 as the two reporters of water–protein ^1H exchange in the pore, whereas I14 and A22 are expected to receive magnetization indirectly from other sidechains through ^1H spin diffusion along the protein backbone.

At acidic pH, we find S/S_0 values of less than 0.21 for the S12, I14, and A22 backbone signals, while the H19 C α /C δ 1 intensity is more than twice as high (Fig. 4B), indicating that water magnetization transfer to the H19 sidechain is much faster than to other residues. At neutral pH, lower S/S_0 values are observed. This is opposite the trend of faster chemical exchange at higher pH: for example, hydrogen exchange of NH groups is the slowest at ~pH 3.5, with a minimum value of $\sim 500 \text{ s}^{-1}$ [30–32], and increases by an order of magnitude per pH unit. Chemical exchange of OH protons is the slowest between pH 6 and 6.5, with a minimum value of $\sim 10 \text{ s}^{-1}$ [33]. Compared to chemical exchange, spin diffusion is independent of pH as long as no major protein structural changes occur. Thus, the measured pH dependence of the S/S_0 values indicate that the BM2 channel lumen is better hydrated and more water-accessible at low pH than at high pH.

In addition to the 30 kHz MAS, we also measured water-protein polarization transfer at 13 kHz MAS where spin diffusion along the peptide backbone is faster. Under this condition, chemical exchange is likely rate-limiting for the overall water-protein polarization transfer process, so that the data reports on the average water accessibility of the channel lumen. We used a mixing time of 4 ms for the S experiments to remain in the initial regime of the buildup curve, and found a similar S/S_0 value for the lipid-facing I14 as for the pore-facing S12, consistent with fast ^1H spin diffusion in the peptide (Fig. S5). Notably, the S/S_0 values of these residues are the highest at pH 4.5, decrease from pH 4.5 to pH 5.5, then remain constant from pH 5.5 to pH 7.5. This trend suggests a strong influence of H19, which is highly cationic at pH 4.5 but has a roughly constant charge between pH 5.5 and pH 7.5.

Comparing the mutant and WT channels at the intermediate pH of 5.5, we found that water polarization transfer is faster in the WT (Fig. 4C and Fig. S5). This finding could result from additional water-to-protein magnetization transfer at the second histidine, H27, and/or from increased hydration in the WT channel. As shown below by distance measurements, the presence or absence of H27 does not change the channel diameter, thus suggesting similar channel hydration in both constructs. On the other hand, in WT BM2 H27 shows considerably faster magnetization exchange (Fig. S5F) than H19, which is correlated with the higher average charge of H27 than H19: at pH 5.5 H27 has an average charge of 3.4 ± 0.1 while H19 has an average charge of 1.5 ± 0.1 . The more charged H27 tetrad should promote higher proton conductance, which in turn can cause faster protonation and deprotonation of the imidazole NH-groups [24].

Mutant BM2 has a pH-dependent channel diameter

Complementing the water polarization transfer data, we measured the channel diameter to understand the effects of pH on the helix bundle. The channel diameter is probed at two locations, the C-terminal W23 and the N-terminal F5, using the ^{19}F CODEX technique [34, 35]. The experiments were conducted at low temperatures (243–248 K) to immobilize the sidechains. The ^{19}F spinning sideband intensities of 5F-W23 and 4F-F5 (Fig. S6) indicate

chemical shift anisotropies (CSA) close to the rigid-limit values [36] (Table S3), thus ruling out large- amplitude fast motions at these temperatures.

Fig. 4D, E shows the ^{19}F CODEX decays of 5F-W23 and 4F-F5 in VM+ bound H27A BM2. Biexponential decays were observed. The fast component plateaus within 100–200 ms, and represents 25–30% of the total decay for W23 in the mutant, 15% for W23 in WT BM2, and 45–50% for F5 in the mutant (Fig. S7). For both W23 and F5, neither the amplitude of the fast component nor the ^{19}F linewidth (4.9 ± 0.1 ppm for W23 and 5.6 ± 0.1 ppm for F5) changed with pH, indicating that the origin of the fast component is residual sidechain motion on the 30 – 60 ms timescale, with the F5-containing N-terminus having higher mobility than the W23-containing C-terminus. The major component of the CODEX decay reports the interhelical distances and reaches an equilibrium value of $S/S_0 = 0.25$ after ~ 2 s, consistent with the tetrameric nature of the channel [34]. Importantly, the nearest-neighbor distance between the 5F-W23 sidechains increases from 9.5 ± 0.2 Å at pH 7.5 to 10.2 ± 0.2 Å at pH 5.5 and 10.5 ± 0.2 Å at pH 4.5 (Fig. 4D, E). Therefore, the diagonal distance of the channel at this residue widens by 1.4 Å as the pH decreases from 7.5 to 4.5. This channel widening at low pH correlates with the increased average H19 charge from 0.7 ± 0.1 to 3.1 ± 0.1 over the same pH range. This 10% distance increase is smaller than expected for a conformational change between a closed (C_{closed}) and open (C_{open}) state. We attribute this moderate increase to H19–W23 aromatic interactions, which may regulate the distances between W23 sidechains to less than those dictated by H19–H19 electrostatic repulsion alone. A similarly moderate increase of W41–W41 interhelical distances was also observed in AM2 [37], which can be attributed to the combined effects of H37–H37 electrostatic repulsion and water-mediated W41–D44 hydrogen bonding [26]. In comparison, the ^{19}F CODEX data of Phe5 show no pH-dependent distance change within 2σ confidence intervals: the nearest-neighbor ^{19}F – ^{19}F distances are 9.4 ± 0.2 Å at pH 5.5 and 9.0 ± 0.2 Å at pH 4.5 (Fig. S7), where the uncertainties correspond to 1σ standard deviation. Therefore, the channel diameter at this N-terminal helix-to-coil transition point is insensitive to pH between pH 5.5 and 4.5. Although this pH range is small, our experimental observation is supported by very recent molecular dynamics simulations [28] that showed that with decreasing pH, the BM2 channel diameter increased at the H19xxxW23xxxH27 motif while interhelical distances in the N-terminal region remain unaffected.

To investigate if H27 affects the C-terminal channel diameter, we compared the W23 interhelical distances in the WT and the mutant at pH 5.5 (Fig. 4E, F). The same distance of 10.2 ± 0.2 Å was found for both samples, indicating that the identity of residue 27 does not affect the channel diameter at W23. At pH 5.5, the H19 tetrad carries an average charge of +1.5 in both the mutant and WT BM2, but the WT peptide has another +3.5 charges at H27, which give a total charge of +5.0 for the four-helix bundle. Thus, the fact that the W23 channel diameter is similar between the WT and mutant indicates that electrostatic repulsion between the pore-facing H19 sidechains drives the pH-dependent channel widening, whereas H27 at the membrane surface has too weak electrostatic repulsion to influence the channel diameter.

Conclusions

The solid-state NMR data shown here provide novel insights into the structural and dynamical interplay between multiple polar residues of a membrane-bound ion channel in regulating proton transfer. By mutating the second histidine of BM2 to a hydrophobic alanine, we created the same HxxxW conduction motif for BM2 as for AM2. The H19 chemical shifts reveal that this single-histidine BM2 variant resembles the single-histidine AM2 structural phenotype, despite the fact that the rest of the BM2 pore is drastically different from the AM2 pore. This single-histidine phenotype is characterized by a dominant +1 and +2 charge in a wide pH range of 7.5 to 5.5 (Fig. 3), whereas the double-histidine WT BM2 achieves the dominant +2 charge at lower pH. The second histidine in WT BM2 indeed facilitates proton release from H19 and shifts its protonation equilibrium to lower pH (Fig. 5a), which is also concluded from MD simulations [28]. These data indicate that H27 in the symmetric H¹⁹xxxW²³xxxH²⁷ motif of WT BM2 is responsible for the higher inward proton conductance of BM2 compared to AM2. In addition, the mutant H19 shows a shifted tautomeric equilibrium towards the τ tautomer, which also resembles the tautomeric equilibrium of H37 in WT AM2. This observation suggests that the large π tautomer population in WT BM2 is a direct reflection of the reverse current of the channel. The membrane-surface H27 is protonated at higher pH than the interior H19 [21], therefore it can create a proton motive force from the C-terminus to the N-terminus at moderate pH. Such a proton chemical potential is absent in AM2, because R45 is not titratable at physiological pH. Together, these results indicate that the H¹⁹xxxW²³xxxH²⁷ motif is effectively a double conductance motif: H19 is responsible for channel activation and functional inward conductance, whereas H27 enhances both the inward conductance and the outward conductance at moderate pH.

Decreasing the pH increased the channel diameter at the gating W23 by 1.4 Å, and this widening is exclusively correlated with the H19 tetrad charge but not the H27 charge. At low pH, the single-histidine mutant BM2 has overall similar water accessibilities between the N- and C- terminal regions, whereas the double-histidine WT BM2 exhibits faster proton exchange at the C-terminus, consistent with the presence of the additional titratable H27. Comparing the data to the histidine charge state reveals that water–protein proton exchange correlates with the average histidine charge.

These results demonstrate that H27 is a pH- and charge-dependent trigger for increasing the proton conductance in the H¹⁹xxxW²³ dyad. The fact that H27 changes the protonation behavior of H19 despite a long C α –C α distance of ~11 Å strongly suggests cation– π interactions of both histidines with W23. The 1.5-fold higher conductance in the presence of H27 [29, 38, 39] emphasizes the synergistic effects of H19 and H27. Such proton relay between two remote polar residues may also be present in other ion channels such as the Hv channel. Structural insights from the current study can facilitate the development of synthetic proton-selective water channels for energy-efficient water desalination, where multiple imidazole tetrads have been stacked together to mediate water and proton conduction [40, 41].

Materials and Methods

Solid-phase peptide synthesis of site-specific labeled H27A BM2 (1–33)

BM2 (1–33) H27A (MLEPFQILSI SSFILSALHF MAWTIGALNQ IKR) of the B/Maryland/1/2001 strain of the influenza virus was synthesized by Fmoc solid-phase peptide synthesis (SPPS) using a custom-designed flow synthesizer [42, 43]. Uniformly ^{13}C , ^{15}N -labeled S12, I14, H19, A22, 4- ^{19}F -labeled F5, and 5- ^{19}F -labeled W23 were incorporated into the sequence. SPPS of BM2 (1–33) H27A was conducted on H-Rink amide ChemMatrix® resin. 0.075 mmol resin (0.15 g at 0.5 mmol/g loading size) was swelled in the reaction syringe for 5 min in ~5 mL N, N-dimethylformamide (DMF) at 70°C. Ten-fold excess (0.75 mmol) unlabeled amino acids and four-fold excess (0.3 mmol) labeled amino acids were singly and doubly coupled with a coupling time of 50 s and 70 s, respectively. To reduce racemization in the process of histidine coupling, H19 was manually coupled at room temperature for 1 h [44]. After the last coupling step, the peptide was deprotected and cleaved from the resin by addition of a TFA / phenol / water / TIPS solution (88 : 5 : 5 : 2 by volume) for 3 h. The resin was filtered, and the crude peptide was precipitated and triturated three times with cold diethyl ether, then dried under vacuum at room temperature for an hour. The dried crude peptide was dissolved in 50% acetonitrile solution and purified by preparative RP-HPLC using a Vydac C4 column with a linear gradient of 40–90% (channel A) over 90 min at a flow rate of 10 mL/min (channel A: acetonitrile; channel B: water). MALDI-MS analysis confirmed the mass to be 3836.2 Da, in excellent agreement with the calculated mass of 3836.5 Da. The combined synthesis and purification yield was ~7%.

Membrane protein samples for SSNMR

H27A BM2(1–33) was reconstituted into a VM+ membrane, which contains 1-palmitoyl-2-oleoyl-*sn*-glycero-3-phosphocholine (POPC), 1-palmitoyl-2-oleoyl-*sn*-glycero-3-phosphoethanolamine (POPE), sphingomyelin (SPM), and cholesterol at a molar ratio of 25 : 25 : 25 : 25. All lipids were dissolved in ~500 μl chloroform, and 4 μl of methanol was added to the lipid solution to dissolve SPM. The peptide was dissolved in ~300 μl 2,2,2-trifluoroethanol (TFE) and mixed with the lipid solution. The peptide : lipid molar ratio was 1 : 14.5. The solvents were mostly removed under nitrogen gas. Then, the samples were completely dried under room temperature vacuum overnight. The dried lipid/peptide samples were resuspended in different buffers based on the pH of each sample and dialyzed against the relevant buffers with five buffer exchanges to remove salt and residual TFA and TFE. The proteoliposomes were spun at 40,000 rpm using a Beckman SW60T rotor at 4°C for 4 h to obtain wet membrane pellets. The pellets were incubated in a desiccator until it reached a hydration content of ~40 wt% water by mass and then spun into magic-angle spinning (MAS) rotors to conduct solid-state NMR experiments.

Control of the membrane pH was crucial for accurate determination of the H19 pK_a 's. We measured the pH of the solutions at several stages during the membrane sample preparation: the buffer immediately before its addition to the lyophilized peptide/lipid mixture, and the supernatant after ultracentrifugation. Reported pH values and uncertainties are the average and standard deviation of these measurements. Five samples at different pH values were prepared using the following buffers: pH 4.5 ± 0.1 (20 mM citric acid, 2 mM EDTA, 0.2

mM NaN₃), pH 5.0 ± 0.1 (20 mM citric acid, 2 mM EDTA, 0.2 mM NaN₃), pH 5.5 ± 0.1 (20 mM citric acid, 2 mM EDTA, 0.2 mM NaN₃), pH 6.5 ± 0.1 (20 mM Bis-Tris/HCl, 2 mM EDTA, 0.2 mM NaN₃), pH 7.5 ± 0.2 (20 mM HEPES/NaOH, 2 mM EDTA, 0.2 mM NaN₃).

Solid-state NMR experiments

SSNMR spectra were measured on Bruker NMR spectrometers at 9.4 T (400 MHz ¹H Larmor frequency) and 14.1 T (600 MHz ¹H frequency) using a 4 mm ¹H/¹³C/¹⁵N MAS probe, a 4 mm ¹H/¹⁹F/¹³C probe and a 1.9 mm ¹H/¹⁹F/¹³C probe. ¹³C chemical shifts were externally referenced to the adamantane CH₂ signal at 38.48 ppm on the tetramethylsilane scale, whereas ¹⁵N chemical shifts were referenced to the amide signal of N-acetylvaline at 122.0 ppm on the liquid ammonia scale. ¹⁹F chemical shifts were referenced to the ¹⁹F signal of Teflon at -122 ppm. Sample temperatures are thermocouple-reported values without correcting for MAS frictional heating.

1D ¹³C and ¹⁵N CP MAS spectra were measured at 9.4 T from 243 K to 263 K under MAS frequencies of 7.0 kHz to 13.5 kHz. Out of the four ¹³C, ¹⁵N labeled residues (S12, I14, H19, A22), only H19 contains nitrogens in its sidechain. 1D ¹⁵N NMR spectra thus contain H19 sidechain peaks (160–250 ppm) and four overlapping ¹⁵N backbone peaks (110–125 ppm; see Fig. 3A), which were not used for data evaluation. The ¹⁵N CP intensity ratio of protonated vs. unprotonated H19 sidechain peaks, $I_{\text{NH}}/I_{\text{N}}$, was used to quantify the neutral-to-charge histidine concentration ratio by taking into account the different ¹H–¹⁵N polarization transfer efficiencies for protonated and unprotonated ¹⁵N peaks,

$$\frac{[\text{His}]}{[\text{HisH}^+]} = \frac{2}{(I_{\text{NH}}/I_{\text{N}})/\kappa - 1} \quad (1)$$

The CP correction factor, $\kappa = I^{\text{His,NH}}/I^{\text{His,N}}$, was measured before each ¹⁵N experiment by measuring the ¹⁵N CP signal of histidine at pH 8.5 under the same CP matching condition as used for the peptide. The κ values range from 1.13 to 1.19, thus they have less than 5% variation between different experiments. In all experiments, the unprotonated ¹⁵N signal was maximized using a CP contact time of 3 ms.

The four acid dissociation constants of the His tetrad, $K_{\text{a}1-4}$, were determined from the ¹⁵N NMR spectra using the equation [16, 20, 24]

$$P = \frac{[\text{His}]}{[\text{HisH}^+]} = \frac{1 \cdot \frac{K_{\text{a}1}}{10^{-\text{pH}}} + 2 \cdot \frac{K_{\text{a}1} \cdot K_{\text{a}2}}{10^{-2\text{pH}}} + 3 \cdot \frac{K_{\text{a}1} \cdot K_{\text{a}2} \cdot K_{\text{a}3}}{10^{-3\text{pH}}} + 4 \cdot \frac{K_{\text{a}1} \cdot K_{\text{a}2} \cdot K_{\text{a}3} \cdot K_{\text{a}4}}{10^{-4\text{pH}}}}{4 + 3 \cdot \frac{K_{\text{a}1}}{10^{-\text{pH}}} + 2 \cdot \frac{K_{\text{a}1} \cdot K_{\text{a}2}}{10^{-2\text{pH}}} + 1 \cdot \frac{K_{\text{a}1} \cdot K_{\text{a}2} \cdot K_{\text{a}3}}{10^{-3\text{pH}}}} \quad (2)$$

The χ^2 deviation between the calculated ($P_{\text{calc},i}$) and experimental ($P_{\text{exp},i}$) histidine population ratios is defined as

$$\chi^2 = \nu^{-1} \sum_i (P_{\text{exp},i} - P_{\text{calc},i})^2 / \sigma_{\text{exp},i}^2 \quad (3)$$

Eq. (3) accounts for the experimental uncertainty ($\sigma_{\text{exp},i}$) in the measured histidine population ratio and the degree of freedom of the parameter adjustment (ν), i.e., the difference between the number of experimental data points and the number of adjustable parameters. For our experiments $\nu = 1$. Once the pK_a values are determined, the pH-dependent charge population of the channel, termed N_{+1-4} , are obtained using [16]

$$\begin{aligned} N_{+4} &= [\text{H}^+]^4 / \Sigma_N & (4) \\ N_{+3} &= [\text{H}^+]^3 K_1 / \Sigma_N \\ N_{+2} &= [\text{H}^+]^2 K_1 K_2 / \Sigma_N \\ N_{+1} &= [\text{H}^+] K_1 K_2 K_3 / \Sigma_N \\ N_{+0} &= K_1 K_2 K_3 K_4 / \Sigma_N \end{aligned}$$

where Σ_N is a normalization constant such that $\sum_{i=0}^4 N_{+i} = 1$.

2D ^{13}C - ^{13}C correlation spectra were measured using DARR irradiation [45] with 70 ms mixing to assign the ^{13}C chemical shifts at 9.4 T and 243–263 K. ^{19}F CODEX experiments performed at low temperature were used to measure intermolecular ^{19}F - ^{19}F distances based upon the decay rate of the CODEX signal with increasing spin exchange time. These experiments were conducted either at 9.4 T and 243 K under 10 kHz MAS, or at 14.1 T and 248 K under 17.5 kHz MAS [34, 35]. ^{19}F T_1 relaxation effects were corrected for by evaluating the intensity ratio of a control experiment (S_0) and a dephasing experiment (S), alternatingly measured with the same total number of scans. The ^{19}F CODEX decay curves were fit to a biexponential decay, the majority component of which was compared to simulated CODEX curves calculated using a MATLAB program that employs an exchange matrix to treat spin diffusion in a four-spin system [34]. Rate constants (k_{ij}) in the 4×4 exchange matrix are proportional to the squared ^{19}F - ^{19}F dipolar coupling strength (ω_{ij}^2) and hence the internuclear distance (r_{ij}), where

$$k_{ij} = 0.5\pi\omega_{ij}^2 F_{ij}(0) \quad (5)$$

and

$$\omega_{ij} = 0.8 \cdot \frac{\mu_0}{4\pi} \gamma^2 \hbar \cdot r_{ij}^{-3} \quad (6)$$

The rate constants also depend on the overlap integral, $F_{ij}(0)$, whose value has been measured to be 41 μs at 9.4 T and 8 kHz MAS [34] and 21 μs at 14.1 T and 17.5 kHz MAS [46]. ^{19}F CSA parameters were determined by Herzfeld-Berger analysis [47] of spinning sidebands and fitting SIMPSON simulations [48] to the ^{19}F spectrum at 243 K.

^{13}C -detected water-to-protein ^1H spin diffusion experiments were conducted to measure the water accessibility of the mutant channel (see Fig. S8 for the pulse sequence). The experiment used a ^1H Gaussian 90° pulse of 2 ms at 14.1 T and 3 ms at 9.4 T to selectively excite the ^1H water signal. Experiments were conducted either at 30 kHz or 13 kHz MAS to make use of different ^1H spin diffusion efficiencies. Residual ^1H magnetization of the peptide and the lipid was removed using a ^1H T_2 filter of $35 \mu\text{s} \times 2$, followed by a ^1H polarization exchange period between 2 ms and 100 ms [49]. To extract the initial spin diffusion buildup intensity (S/S_0), we used spectra after 9 ms spin exchange at 30 kHz MAS (4 ms exchange at 13 kHz MAS; S experiment), and after 100 ms spin exchange (S_0). The short mixing time minimizes ^1H spin diffusion among peptide protons after the water-to-protein polarization transfer and allows to access to the spin polarization exchange rate. The degree of residual spin diffusion along the protein backbone can be estimated using a 1D model of spin diffusion along the protein backbone [50]. At slow MAS, where spin diffusion along the protein backbone is considerable, the mean displacements of ^1H polarization after 4 ms mixing is in the range from 9 \AA to 25 \AA for diffusion coefficients of 0.1 – 0.8 nm^2/ms [51–53]. To minimize spectral overlap in the 1D ^{13}C spectrum, we focused the data evaluation on the well resolved Ca peaks of S9/S12, I14, and A22, as well as on the combined Ce1 and C δ 1 peaks of H19.

Supplementary Material

Refer to Web version on PubMed Central for supplementary material.

Acknowledgments

This work is supported by NIH grant GM088204 to M.H. and a German National Academy of Sciences Leopoldina postdoctoral fellowship (LPDS-2017–14) to M.R.

References

- [1]. Ramsey IS, Moran MM, Chong JA, Clapham DE. A voltage-gated proton-selective channel lacking the pore domain. *Nature*. 2006;440:1213–6. [PubMed: 16554753]
- [2]. DeCoursey TE. Voltage-gated proton channels: molecular biology, physiology, and pathophysiology of the H(V) family. *Physiological reviews*. 2013;93:599–652. [PubMed: 23589829]
- [3]. Cherny VV, Morgan D, Musset B, Chaves G, Smith SM, DeCoursey TE. Tryptophan 207 is crucial to the unique properties of the human voltage-gated proton channel, hHV1. *The Journal of general physiology*. 2015;146:343–56. [PubMed: 26458876]
- [4]. Christianson DW, Fierke CA. Carbonic anhydrase: Evolution of the zinc binding site by nature and by design. *Accounts Chem Res*. 1996;29:331–9.
- [5]. Tu CK, Silverman DN, Forsman C, Jonsson BH, Lindskog S. Role of histidine 64 in the catalytic mechanism of human carbonic anhydrase II studied with a site-specific mutant. *Biochemistry-US*. 1989;28:7913–8.

- [6]. Pinto LH, Holsinger LJ, Lamb RA. Influenza virus M2 protein has ion channel activity. *Cell*. 1992;69:517–28. [PubMed: 1374685]
- [7]. Paterson RG, Takeda M, Ohigashi Y, Pinto LH, Lamb RA. Influenza B virus BM2 protein is an oligomeric integral membrane protein expressed at the cell surface. *Virology*. 2003;306:7–17. [PubMed: 12620792]
- [8]. Pinto LH, Lamb RA. The M2 proton channels of influenza A and B viruses. *J Biol Chem*. 2006;281:8997–9000. [PubMed: 16407184]
- [9]. Bright RA, Medina MJ, Xu XY, Perez-Oronoz G, Wallis TR, Davis XHM, et al. Incidence of adamantane resistance among influenza A (H3N2) viruses isolated worldwide from 1994 to 2005: a cause for concern. *Lancet*. 2005;366:1175–81. [PubMed: 16198766]
- [10]. Wang C, Lamb RA, Pinto LH. Activation of the M2 ion channel of influenza virus: a role for the transmembrane domain histidine residue. *Biophys J*. 1995;69:1363–71. [PubMed: 8534806]
- [11]. Tang Y, Zaitseva F, Lamb RA, Pinto LH. The Gate of the Influenza Virus M2 Proton Channel Is Formed by a Single Tryptophan Residue. *J Biol Chem*. 2002;277:39880–6. [PubMed: 12183461]
- [12]. Hong M, Fritzsche KJ, Williams JK. Hydrogen-bonding partner of the proton-conducting histidine in the influenza M2 proton channel revealed from 1H chemical shifts. *J Am Chem Soc*. 2012;134:14753–5. [PubMed: 22931093]
- [13]. Liao SY, Yang Y, Tietze D, Hong M. The influenza m2 cytoplasmic tail changes the proton-exchange equilibria and the backbone conformation of the transmembrane histidine residue to facilitate proton conduction. *J Am Chem Soc*. 2015;137:6067–77. [PubMed: 25892574]
- [14]. Thomaston JL, Alfonso-Prieto M, Woldeyes RA, Fraser JS, Klein ML, Fiorin G, et al. High-resolution structures of the M2 channel from influenza A virus reveal dynamic pathways for proton stabilization and transduction. *Proc Natl Acad Sci USA*. 2015;12:14260–5.
- [15]. Acharya A, Carnevale V, Fiorin G, Levine BG, Polishchuk A, Balannick V, et al. Structural mechanism of proton transport through the influenza A M2 protein. *Proc Natl Acad Sci USA*. 2010;107:15075–80. [PubMed: 20689043]
- [16]. Hu FH, Schmidt-Rohr K, Hong M. NMR Detection of pH-Dependent Histidine-Water Proton Exchange Reveals the Conduction Mechanism of a Transmembrane Proton Channel. *J Am Chem Soc*. 2012;134:3703–13. [PubMed: 21974716]
- [17]. Hu F, Luo W, Hong M. Mechanisms of Proton Conduction and Gating in Influenza M2 Proton Channels from Solid-State NMR. *Science*. 2010;330:505–8. [PubMed: 20966251]
- [18]. Hu J, Fu R, Nishimura K, Zhang L, Zhou HX, Busath DD, et al. Histidines, heart of the hydrogen ion channel from influenza A virus: toward an understanding of conductance and proton selectivity. *Proc Natl Acad Sci USA*. 2006;103:6865–70. [PubMed: 16632600]
- [19]. Colvin MT, Andreas LB, Chou JJ, Griffin RG. Proton association constants of His 37 in the Influenza-A M218–60 dimer-of-dimers. *Biochemistry-U.S.* 2014;53:5987–94.
- [20]. Williams JK, Tietze D, Lee M, Wang J, Hong M. Solid-State NMR Investigation of the Conformation, Proton Conduction, and Hydration of the Influenza B Virus M2 Transmembrane Proton Channel. *J Am Chem Soc*. 2016;138:8143–55. [PubMed: 27286559]
- [21]. Williams JK, Shcherbakov AA, Wang J, Hong M. Protonation equilibria and pore-opening structure of the dual-histidine influenza B virus M2 transmembrane proton channel from solid-state NMR. *J Biol Chem*. 2017;292:17876–84. [PubMed: 28893910]
- [22]. Wang J, Pielak RM, McClintock MA, Chou JJ. Solution structure and functional analysis of the influenza B proton channel. *Nat Struct Mol Biol*. 2009;16:1267–71. [PubMed: 19898475]
- [23]. Ma C, Soto CS, Ohigashi Y, Taylor A, Bournas V, Glawe B, et al. Identification of the Pore-lining Residues of the BM2 Ion Channel Protein of Influenza B Virus. *J Biol Chem*. 2008;283:15921–31. [PubMed: 18408016]
- [24]. Mandala VS, Liao SY, Kwon B, Hong M. Structural Basis for Asymmetric Conductance of the Influenza M2 Proton Channel Investigated by Solid-State NMR Spectroscopy. *J Mol Biol*. 2017;429:2192–210. [PubMed: 28535993]
- [25]. Schnell JR, Chou JJ. Structure and mechanism of the M2 proton channel of influenza A virus. *Nature*. 2008;451:591–5. [PubMed: 18235503]

- [26]. Ma C, Fiorin G, Carnevale V, Wang J, Lamb RA, Klein ML, et al. Asp44 stabilizes the Trp41 gate of the M2 proton channel of influenza A virus. *Structure*. 2013;21:2033–41. [PubMed: 24139991]
- [27]. Ma C, Wang J. Functional studies reveal the similarities and differences between AM2 and BM2 proton channels from influenza viruses. *Biochim Biophys Acta*. 2018;1860:272–80.
- [28]. Zhang YL, Zhang HX, Zheng QC. A unique activation-promotion mechanism of the influenza B M2 proton channel uncovered by multiscale simulations. *Phys Chem Chem Phys*. 2019;21:2984–91. [PubMed: 30672572]
- [29]. Otomo K, Toyama A, Miura T, Takeuchi H. Interactions Between Histidine and Tryptophan Residues in the BM2 Proton Channel from Influenza B Virus. *J Biochem*. 2009;145:543–54. [PubMed: 19155268]
- [30]. Bai Y, Milne JS, Mayne L, Englander SW. Primary structure effects on peptide group hydrogen exchange. *Proteins*. 1993;17:75–86. [PubMed: 8234246]
- [31]. Henry GD, Sykes BD. Determination of the rotational dynamics and pH dependence of the hydrogen exchange rates of the arginine guanidino group using NMR spectroscopy. *J Biomol NMR*. 1995;6:59–66. [PubMed: 22911578]
- [32]. Sehgal AA, Duma L, Bodenhausen G, Pelupessy P. Fast proton exchange in histidine: measurement of rate constants through indirect detection by NMR spectroscopy. *Chemistry*. 2014;20:6332–8. [PubMed: 24719307]
- [33]. Liepinsh E, Otting G, Wuthrich K. NMR spectroscopy of hydroxyl protons in aqueous solutions of peptides and proteins. *J Biomol NMR*. 1992;2:447–65. [PubMed: 1384851]
- [34]. Luo W, Hong M. Determination of the oligomeric number and intermolecular distances of membrane protein assemblies by anisotropic ^1H -driven spin diffusion NMR spectroscopy. *J Am Chem Soc*. 2006;128:7242–51. [PubMed: 16734478]
- [35]. deAzevedo ER, Hu WG, Bonagamba TJ, Schmidt-Rohr K. Centerband-only detection of exchange: Efficient analysis of dynamics in solids by NMR. *J Am Chem Soc*. 1999;121:8411–2.
- [36]. Dürr HN, Grage SL, Witter R, Ulrich AS. Solid state ^{19}F NMR parameters of fluorine- labeled amino acids. Part I: Aromatic substituents. *J Magn Reson*. 2008;191:7–15. [PubMed: 18155936]
- [37]. Williams JK, Zhang Y, Schmidt-Rohr K, Hong M. pH-Dependent Conformation, Dynamics, and Aromatic Interaction of the Gating Tryptophan Residue of the Influenza M2 Proton Channel from Solid-State NMR. *Biophys J*. 2013;104:1698–708. [PubMed: 23601317]
- [38]. Ma CL, Soto CS, Ohigashi Y, Taylor A, Bournas V, Glawe B, et al. Identification of the pore-lining residues of the BM2 ion channel protein of influenza B virus. *J Biol Chem*. 2008;283:15921–31. [PubMed: 18408016]
- [39]. Wang JF, Pielak RM, McClintock MA, Chou JJ. Solution structure and functional analysis of the influenza B proton channel. *Nat Struct Mol Biol*. 2009;16:1267–U82. [PubMed: 19898475]
- [40]. Barboiu M, Le Duc Y, Gilles A, Cazade PA, Michau M, Marie Legrand Y, et al. An artificial primitive mimic of the Gramicidin-A channel. *Nature communications*. 2014;5:4142.
- [41]. Le Duc Y, Michau M, Gilles A, Gence V, Legrand YM, van der Lee A, et al. Imidazole- quartet water and proton dipolar channels. *Angew Chem Int Ed Engl*. 2011;50:11366–72. [PubMed: 22002728]
- [42]. Simon MD, Heider PL, Adamo A, Vinogradov AA, Mong SK, Li XY, et al. Rapid Flow- Based Peptide Synthesis. *Chembiochem*. 2014;15:713–20. [PubMed: 24616230]
- [43]. Kwon B, Lee M, Waring AJ, Hong M. Oligomeric Structure and Three-Dimensional Fold of the HIV gp41 Membrane-Proximal External Region and Transmembrane Domain in Phospholipid Bilayers. *J Am Chem Soc*. 2018;140:8246–59. [PubMed: 29888593]
- [44]. Kwon B, Tietze D, White PB, Liao SY, Hong M. Chemical ligation of the influenza M2 protein for solid-state NMR characterization of the cytoplasmic domain. *Prot Sci*. 2015;24:1087–99.
- [45]. Takegoshi K, Nakamura S, Terao T. ^{13}C - ^1H dipolar-assisted rotational resonance in magic- angle spinning NMR. *Chem Phys Lett*. 2001;344:631–7.
- [46]. Roos M, Wang T, Shcherbakov AA, Hong M. Fast Magic-Angle-Spinning (^{19}F) Spin Exchange NMR for Determining Nanometer (^{19}F - ^{19}F) Distances in Proteins and Pharmaceutical Compounds. *J Phys Chem B*. 2018;122:2900–11 [PubMed: 29486126]
- [47]. Eichele K HBA 1.7.5 ed: Universität Tübingen; 2015.

- [48]. Bak M, Rasmussen JT, Nielsen NC. SIMPSON: A general simulation program for solid- state NMR spectroscopy. *J Magn Reson.* 2000;147:296–330. [PubMed: 11097821]
- [49]. Mandala VS, Gelenter MD, Hong M. Transport-Relevant Protein Conformational Dynamics and Water Dynamics on Multiple Time Scales in an Archetypal Proton Channel: Insights from Solid-State NMR. *J Am Chem Soc.* 2018;140:1514–24. [PubMed: 29303574]
- [50]. Roos M, Micke P, Hempel G. Monitoring nuclear spin-flip processes and measuring spin-diffusion constants via hole burning into the magnetization. *Chem Phys Lett.* 2012;536:147–54.
- [51]. Clauss J, Schmidt-Rohr K, Spiess HW. Determination of Domain Sizes in Heterogeneous Polymers by Solid-State Nmr. *Acta Polym.* 1993;44:1–17.
- [52]. Roos M, Micke P, Saalwachter K, Hempel G. Moderate MAS enhances local (1)H spin exchange and spin diffusion. *J Magn Reson.* 2015;260:28–37. [PubMed: 26397218]
- [53]. Schneider H, Saalwachter K, Roos M. Complex Morphology of the Intermediate Phase in Block Copolymers and Semicrystalline Polymers As Revealed by H-1 NMR Spin Diffusion Experiments. *Macromolecules.* 2017;50:8598–610.

Highlights

- Wild-type influenza BM2 has two histidines in the transmembrane proton channel.
- The central proton-selective histidine has depressed pK_a 's compared to AM2.
- Removal of the peripheral histidine restores the pK_a of the central histidine.
- Removal of the peripheral histidine shifts the tautomeric equilibrium of the central histidine.
- The peripheral histidine increases both forward and reverse proton conductance, by proton relay with the central histidine.

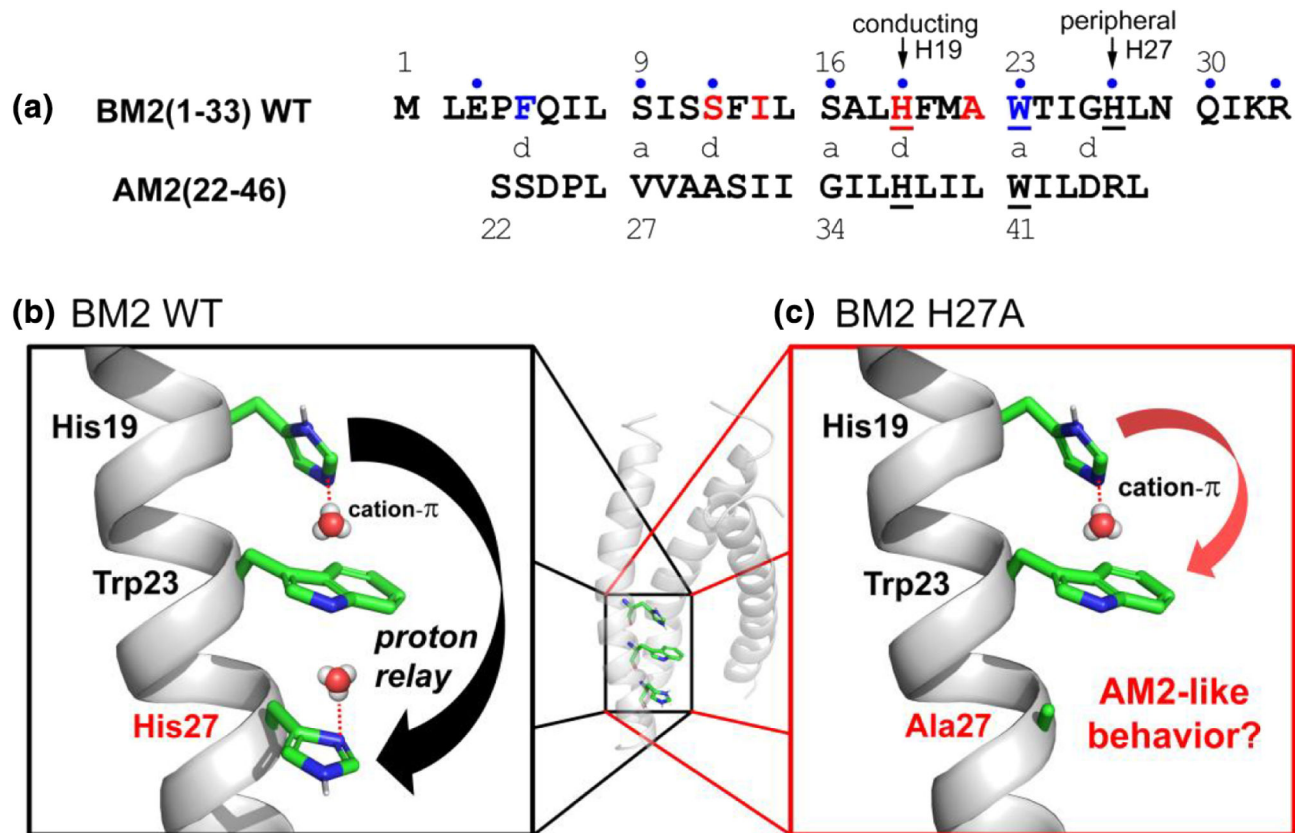


Figure 1.

Amino acid sequence and structural hypotheses of proton conduction in BM2. (A) Sequence alignment of BM2(1–33) relative to AM2(22–46). Pore-facing heptad repeat positions (a,d) are indicated, ¹³C, ¹⁵N-labeled residues are highlighted in red and fluorinated residues are shown in blue. BM2(1–33) WT sidechains expected to be amenable to proton exchange with water are marked with a blue dot. (B) In WT BM2(1–33) (PDB: 2KIX), H27 may facilitate proton dissociation of H19 via cation- π interactions with the central W23. (C) The H27A mutation is designed to remove the possibility of this long-range proton relay, and its effect on the H19 structure, channel hydration and channel diameter, is investigated in this study.

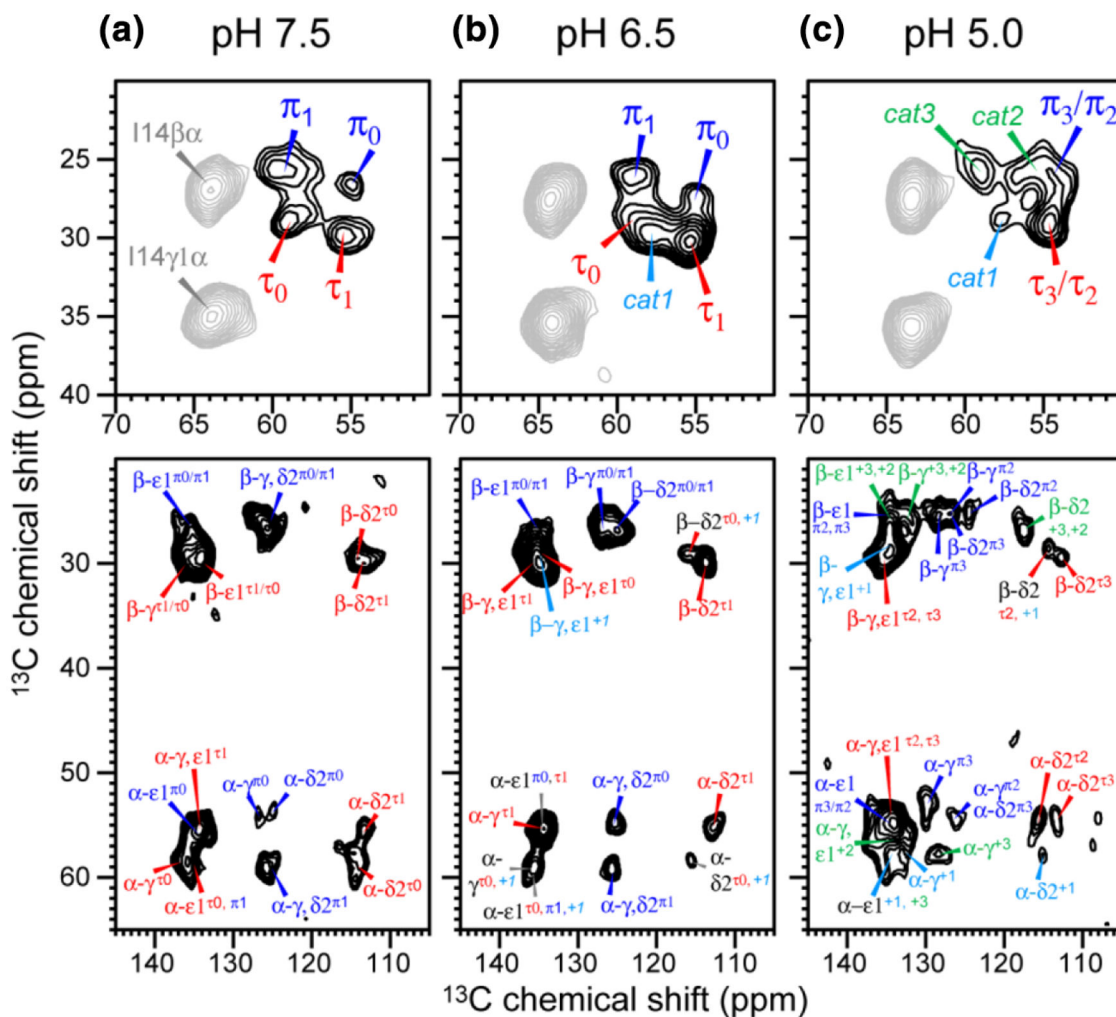


Figure 2.

Aliphatic and aromatic regions of the 2D ^{13}C - ^{13}C correlation spectra of H19 in the mutant BM2 at different pH. All spectra were measured at 243 K. (A) pH 7.5, (B) pH 6.5, and (C) pH 5.0. I14 cross peaks serve as a chemical shift reference and are shaded in gray, while H19 peaks report the conformational and charge state of the channel and are shown in black. The τ and π tautomers show high intensities at high pH and are assigned as $\tau_1 - \tau_3$ and $\pi_1 - \pi_3$, depending on the average charge of the tetrad. Cationic histidine signals become dominant at low pH and are assigned as cat1 – cat3. These different states of the C α -C β cross peaks were assigned based on their correlations with the imidazole sidechain ^{13}C signals.

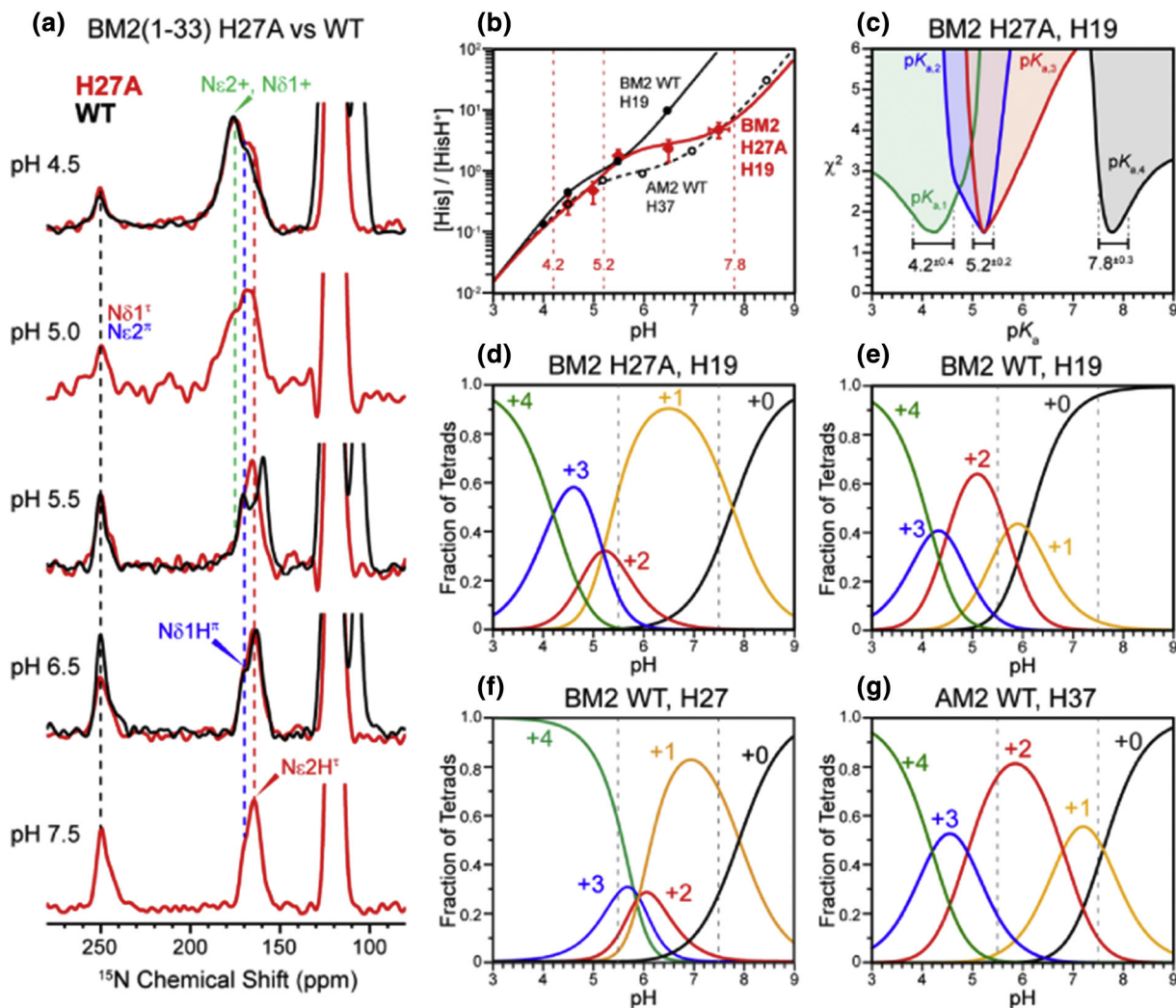


Figure 3.

pH-dependent protonation states and charge distribution of H19, H27 and H37 in BM2 and AM2 channels. (A) ^{15}N spectra as a function of pH for the H19 sidechain in H27A (red) versus WT BM2 (black) [20, 21] bound to the VM+ membrane. Peak intensities reveal the ratio of neutral histidine to cationic histidine. (B) Concentration ratio of neutral-to-cationic H19 (red) calculated from the integrated intensity ratio of protonated and unprotonated ^{15}N peaks after CP correction. The H19 data of the BM2 mutant is superimposed with the H19 data in WT BM2 (black, filled) and the H37 data in AM2 WT [16] (black, open). The H19 pK_a values in the mutant are indicated by vertical lines. Except for pH 7.5, the symbol size matches the size of the horizontal error bar. (C) Deviation of the calculated vs. experimental histidine population ratio, χ^2 , of the BM2 mutant as a function of the four pK_a values. For a given pK_a , the combination of the other pK_a 's leads to the shaded areas. $\text{pK}_{a,2}$ and $\text{pK}_{a,3}$ converge to the same value. (D–G) Comparison of pH-dependent tetrad populations of (D) H19 in mutant BM2, (E) H19 in WT BM2, (F) H27 in WT BM2, and (G) H37 in WT AM2. The +1 charged tetrad of H19 in mutant BM2 is dominant between pH 7.5 and 6.

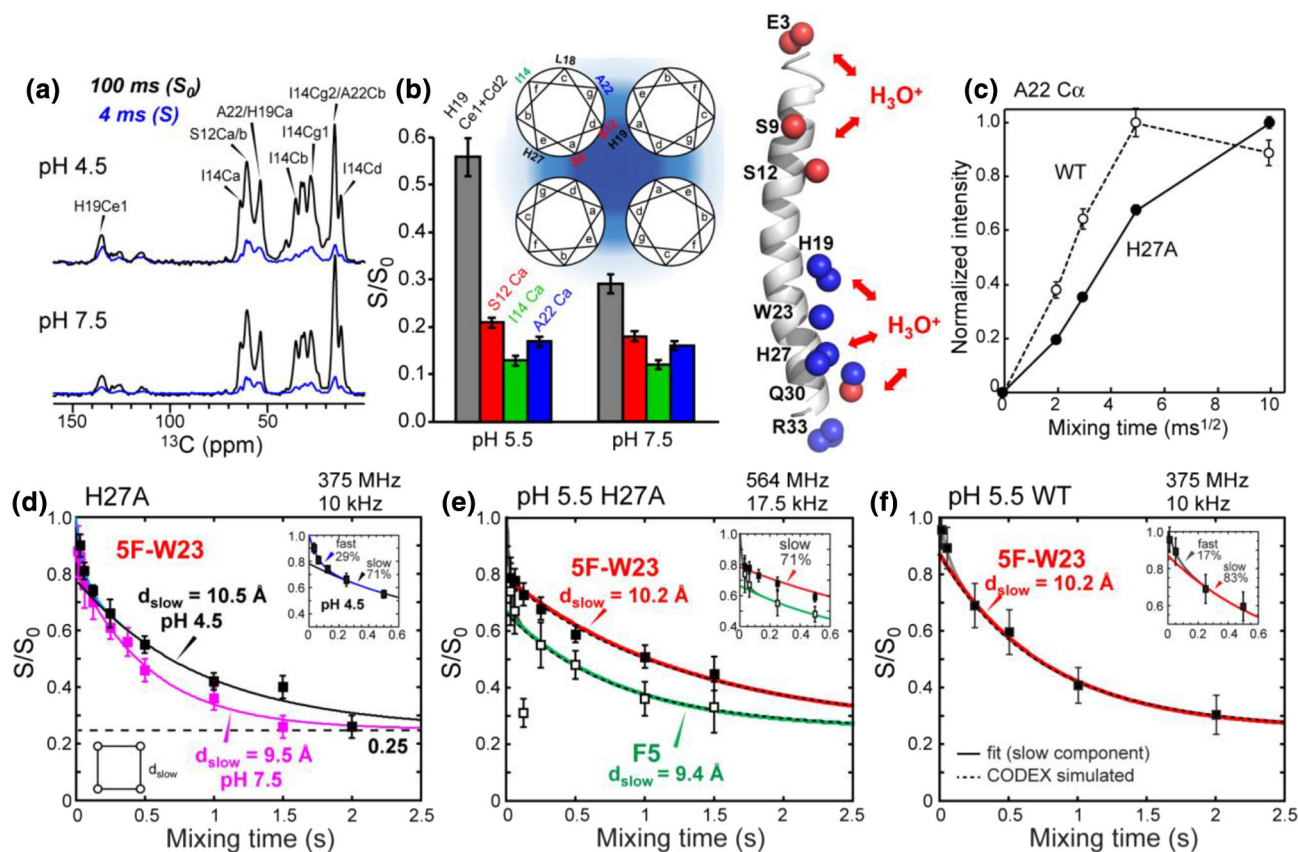


Figure 4.

Hydration and channel width of H27A BM2 as a function of pH. (A) Water-edited ^{13}C spin diffusion spectra of H27A BM2 after 4 ms (S , blue) and 100 ms (S_0 , black) ^1H polarization transfer. (B) S/S_0 ratio of several TM residues at different pH, including heptad repeat positions. Positions of water-exposed OH- or NH-groups along the BM2 helix are highlighted in red and blue, respectively. (C) Comparison of water-to-protein polarization transfer buildup curves of mutant and WT BM2 at pH 5.5. WT BM2 has faster proton exchange and larger hydration than the mutant. (D) ^{19}F CODEX decay curves of 5F-W23 in H27A BM2 at pH 4.5 and pH 7.5. The data were measured at 9.4 T. Associated distances were extracted from the majority component of the bi-exponential decay, while the fast decay (inset) reflects residual motion of the sidechain. (E) 5F-W23 and 4F-F5 CODEX decays at pH 5.5 in H27A BM2. The data were obtained at 14.1 T. (F) 5F-W23 CODEX data of WT BM2 at pH 5.5.

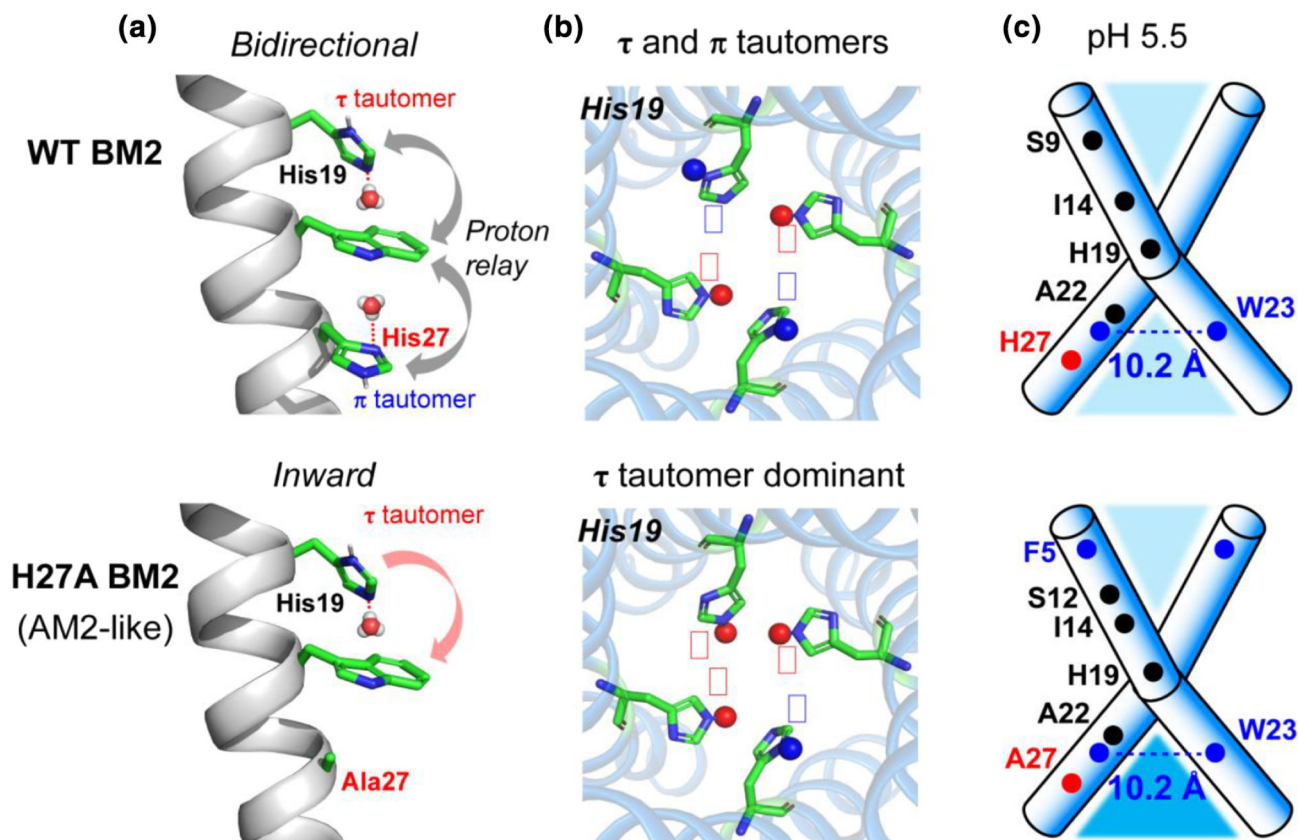


Figure 5.

Effects of H27 on the structure and dynamics of the BM2 proton channel. (A) Proton dissociation of H19 is accelerated by proton relay to H27, most likely mediated by W23. The H27A mutation removes this deprotonation pathway, and reverts H19 to the AM2 H37 behavior. Thus efficient deprotonation in the $H^{19}xxxW^{23}xxxH^{27}$ motif is responsible for the higher conductance of BM2 compared to the $H^{37}xxxW^{41}$ AM2. (B) H27A mutation increases the H19 τ tautomer population compared to π tautomers, indicating that H27 in WT BM2 is responsible for the reverse proton current present in the WT channel. (C) At pH 5.5, the N-terminal channel diameter is the same between WT and mutant BM2, but the WT channel has faster proton exchange with water than the mutant.